RESEARCH ARTICLE

National Science Review
9: nwac095, 2022
https://doi.org/10.1093/nsr/nwac095
Advance access publication 17 May 2022

PHYSICS

Controllable Majorana vortex states in iron-based superconducting nanowires

Chuang Li[1,2], Xun-Jiang Luo[1,2], Li Chen[1,2], Dong E. Liu[3,*], Fu-Chun Zhang[4,5,*] and Xin Liu[1,2,*]

[1]School of Physics and Institute for Quantum Science and Engineering, Huazhong University of Science and Technology, Wuhan 430074, China; [2]Wuhan National High Magnetic Field Center and Hubei Key Laboratory of Gravitation and Quantum Physics, Wuhan 430074, China; [3]State Key Laboratory of Low Dimensional Quantum Physics, Department of Physics, Tsinghua University, Beijing 100084, China; [4]Kavli Institute for Theoretical Sciences and CAS Center for Excellence in Topological Quantum Computing, University of Chinese Academy of Sciences, Beijing 100190, China and [5]Collaborative Innovation Center of Advanced Microstructures, Nanjing University, Nanjing 210093, China

[*]**Corresponding authors.** E-mails: dongeliu@mail.tsinghua.edu.cn; fuchun@ucas.ac.cn; phyliuxin@hust.edu.cn

Received 2 August 2021; **Revised** 15 April 2022; **Accepted** 15 April 2022

ABSTRACT

To reveal the non-Abelian braiding statistics of Majorana zero modes (MZMs), it is crucial to design a Majorana platform, in which MZMs can be easily manipulated in a broad topological nontrivial parameter space. This is also an essential step to confirm their existence. In this study, we propose an iron-based superconducting nanowire system with Majorana vortex states to satisfy desirable conditions. This system has a radius-induced topological phase transition, giving a lower bound for the nanowire radius. In the topological phase, the iron-based superconducting nanowires have only one pair of MZMs over a wide range of radii, chemical potential and external magnetic fields. The wave function of MZMs has a sizable distribution at the side edge of the nanowires. This property enables the control of the interaction of MZMs in neighboring vortex nanowires and paves the way for Majorana fusion and braiding.

Keywords: iron-based superconductor, topological phase transition, superconducting vortex, Majorana zero modes, nanowire

INTRODUCTION

Majorana zero modes (MZMs) have attracted considerable theoretical and experimental attention given their non-Abelian statistics. The physical realization of MZMs can be roughly classified into two: end MZMs in one-dimensional (1D) systems [1–4] and vortex MZMs in two dimensions [5–7]. In pioneering studies, the superconducting proximity effect plays a paramount role in developing experimentally realizable platforms, e.g. superconductor (SC)/semiconductor (Sm) hybrid nanowires [8–11] and Fe chains growing on SCs [12,13] for 1D cases and SC/topological-insulator (SC/TI) heterostructures [14–16] for 2D cases. Despite the impressive progress in the epitaxial growth of SCs [17], the requirement of the ultraclean heterogeneous interface encounters various difficulties in fabrication techniques and experimental measurements [18]. Recent studies have revealed that iron-based superconducting materials simultaneously possess superconductivity and topological energy band structure and can hence support vortex MZMs without fabricating complex heterostructures. Meanwhile, the small Fermi energy and large superconducting gap in iron-based SC enable MZMs to be distinguished from conventional Caroli–de Gennes–Matricon states [19]. These offer great advantages for the experimental realization and detection of MZMs [19–27].

Moreover, observing the zero-bias peak is a necessary but not sufficient condition for detecting MZMs. Perhaps, only the experimental observation of MZM fusion behaviors and braiding statistics can provide the smoking gun signature. Therefore, implementing a Majorana platform optimized for MZM fusion and braiding is the key to the next milestone. Such an optimized platform should satisfy at least three conditions: (1) a broad parameter range to support well-defined topological degeneracy, (2) an efficient control scheme for MZMs and (3) a high fidelity and easy readout scheme. For the vortex MZMs, satisfying the first condition requires precise control of the number of vortex lines in the system, although parameter fine-tuning is unnecessary. The second condition is related to braiding MZMs, which can be intuitively achieved in real space [28], and their physical implementation is challenging for existing experimental

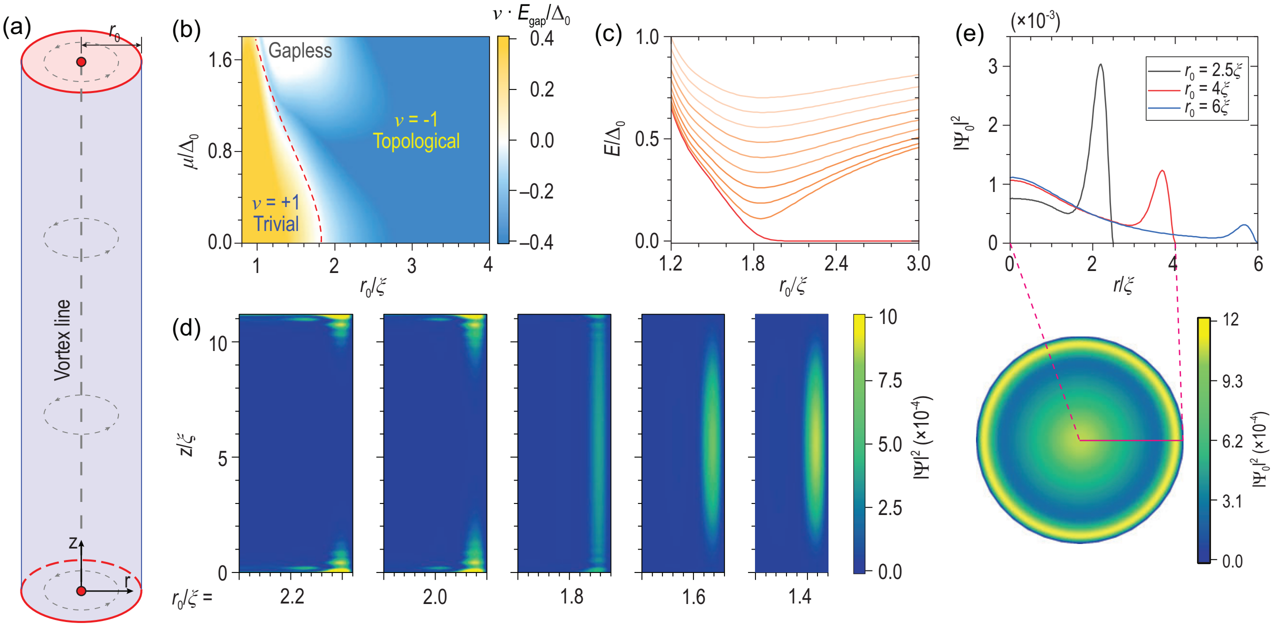

Figure 1. The size effect-induced TPT in the iron-based superconducting nanowire vortex system described by Equation (1). (a) The sketch of an iron-based superconducting nanowire system. (b) The product of the topological invariant ν and the system gap amplitude E_{gap} as a function of the nanowire radius r_0 and chemical potential μ. (c) The variation in the ten lowest positive eigenenergies near the TPT at $\mu = 0$ with open boundary in the z direction. (d) The probability density $|\Psi|^2(r, z)$ of the lowest-energy states in the nanowires with $r_0 = 2.2\xi, \ldots, 1.4\xi$. (e) The distribution of the MZMs' probability density $|\Psi_0|^2$ on the circular surface before the TPT. The parameters used in the calculations are $M = 20$ meV, $A = 30$ meV nm, $A_3 = 2.7$ meV nm, $B = -31$ meV nm^2, $B_3 = 4.7$ meV nm^2, $\Delta_0 = 1.8$ meV so that $\xi \approx 5.3$ nm, and 60 layers spaced by 0.6 nm in the z direction.

techniques. The promising schemes to perform braiding need to control the neighboring Majorana couplings [29–33]. Finally, satisfying the third condition also presupposes a reliable control of Majorana couplings. To the best of our knowledge, there is no detailed physical scheme in the vortex MZM platforms satisfying these three conditions.

In this study, we propose an iron-based superconducting nanowire setup [considering the (001) direction as an example in Fig. 1(a)] to satisfy the three conditions. Because the repulsive interaction exists among vortices with finite distances, there is only a single vortex with one pair of MZMs in a wide range of magnetic fields and radii, causing unambiguous two-fold degenerate ground states. Besides the well-known topological phase transition (TPT) from varying the chemical potential μ [34], we found an additional TPT by tuning the radius r_0 of the iron-based superconducting nanowire. Interestingly, unlike the well-known case, the transition occurs at the chemical potential within the bulk gap. This TPT indicates a lower bound for the nanowire radius that can support MZMs. Moreover, there is a radius range within the topologically nontrivial phase, where the Majorana wave function is distributed with a substantial weight near the vortex center as well as on the nanowire lateral surface. The wave function distribution in the lateral surface allows a gate-tunable coupling between vortex MZMs via their edge contacts. This radius region can be further extended by introducing a local effective Zeeman field (ZF), for example, on the bottom surface where the bottom MZM does not disappear but moves to the bottom edge. This structure is topologically equivalent to a 2D topological SC possessing a single vortex. Notably, one iron-based superconducting nanowire has length l_0 and radius r_0, which allows for proper separation between the bottom and top MZMs while sufficiently maintaining a large gap between the MZMs and Bogoliubov quasiparticle states to prevent quantum information leakage. In parallel to the benefit of achieving MZMs without requiring proximity effects, our scheme embodies great advantages to satisfy the conditions of the optimized Majorana platform. First, the geometry of the nanowires will ensure that there are only two MZMs within a certain radius, thereby providing well-defined doubly degenerated ground states in the Majorana vortex system. Second, the edge MZMs are easily controlled. Third, the next step in non-Abelian statistic studies can be performed using braiding schemes developed from the Sm nanowires.

The rest of this article is organized as follows. First, we discuss the TPT due to the radius of the iron-based superconducting nanowires and the spatial distribution of Majorana vortex modes. Second, to obtain tunable MZMs in a wide range of nanowire radii, we induce a local effective ZF on the bottom surface to push the bottom Majorana vortex to the edge. In addition, we investigate the spectral variation and evolution of MZM wave function. Third, we analyze the gate voltage controllable MZM coupling with and without the local ZF. Then, we discuss the repulsion between vortices in the finite-sized nanowire, which allows the number of MZMs and hence the ground-state degeneracy of the nanowire to be regulated by the magnetic field. Finally, we summarize our results and discuss possible experimental challenges.

TPT AND THE MAJORANA VORTEX WAVE FUNCTION IN AN IRON-BASED SUPERCONDUCTING NANOWIRE

Focusing on the topological band structure near the Fermi surface, the Bogoliubov–de Gennes (BdG) Hamiltonian of the iron-based SC can be expressed as

$$H_{\mathrm{S}} = \begin{pmatrix} H_{\mathrm{TI}}(\boldsymbol{r}) - \mu & \hat{\Delta}_n(\boldsymbol{r}) \\ \hat{\Delta}_n^{\dagger}(\boldsymbol{r}) & -H_{\mathrm{TI}}^{*}(\boldsymbol{r}) + \mu \end{pmatrix}, \quad (1)$$

in the basis $(C(\boldsymbol{r}), C^{\dagger}(\boldsymbol{r}))^T$, with $C(\boldsymbol{r}) = \left(c_{1\uparrow}(\boldsymbol{r}), c_{1\downarrow}(\boldsymbol{r}), c_{2\uparrow}(\boldsymbol{r}), c_{2\downarrow}(\boldsymbol{r})\right)^T$ as the electron annihilation operator in real space; subscripts (1,2) and (↑, ↓) indicate the orbital and spin degrees of freedom, respectively, and μ denotes the chemical potential measured from the Dirac point of the surface states. Here, H_{TI} is expressed as [24,35,36]

$$\begin{aligned} H_{\mathrm{TI}}(\boldsymbol{k}) &= A\hat{\sigma}_x(\hat{s}_x \sin k_x + \hat{s}_y \sin k_y) \\ &\quad + \hat{\sigma}_z[M - B(4 - 2\cos k_x - 2\cos k_y)] \\ &\quad + A_3\hat{\sigma}_x\hat{s}_z \sin k_z - \hat{\sigma}_z B_3(2 - 2\cos k_z) \end{aligned} \quad (2)$$

with M, A, A_3, B and B_3 the anisotropic material parameters, and $\hat{\boldsymbol{\sigma}}$ and $\hat{\boldsymbol{s}}$ the Pauli matrices acting on the orbital and spin spaces, respectively. Because the magnetic field in vortices is small, its effect on bands is neglected. The superconducting term is expressed as

$$\hat{\Delta}_n(\boldsymbol{r}) = -i\hat{s}_y\Delta_0\left(\tanh\left(\frac{r}{\xi}\right)e^{i\varphi}\right)^n, \quad (3)$$

where $n = 0$ (or 1) for a system with no (or one) vortex, Δ_0 denotes the amplitude of the bulk superconducting order parameter and $\xi = \hbar v_F/(\pi\Delta_0)$ denotes the superconducting coherence length with Fermi velocity v_F. For $n = 1$, the chemical potential μ can induce a TPT with the transition above the bulk bandgap [34,36,37]. Remarkably, we found that in the iron-based superconducting nanowires, the size effect, precisely the radius r_0, induces an additional TPT.

We adopt a continuous model in the x-y plane. Then, the system has the continuous rotational symmetry with angular momentum j for H_{S}. For $n = 1$, we block-diagonalize the Hamiltonian with a quantized number $j \in \mathbb{Z}$ in the r-z space as (see the online supplementary material for details)

$$\begin{aligned} &\mathcal{H}^{(j)}(r, z) \\ &= \begin{pmatrix} \mathcal{H}_{\mathrm{TI}}^{(j)} - \mu & -i\hat{s}_y\Delta_0\tanh(r/\xi) \\ i\hat{s}_y\Delta_0\tanh(r/\xi) & -\mathcal{H}_{\mathrm{TI}}^{(-j)^*} + \mu \end{pmatrix}, \end{aligned} \quad (4)$$

where

$$\begin{aligned} \mathcal{H}_{\mathrm{TI}}^{(j)} &= -iA\hat{\sigma}_x\left[\hat{s}_x\partial_r + \frac{i(j+1/2)}{r}\hat{s}_y + \frac{1}{2r}\hat{s}_x\right] \\ &\quad + \hat{\sigma}_z\left(M + B\left[\partial_r^2 + \frac{1}{r}\partial_r \right.\right. \\ &\quad \left.\left. - \frac{1}{r^2}\left(j - \frac{\hat{s}_z - 1}{2}\right)^2\right]\right) \\ &\quad + A_3\hat{\sigma}_x\hat{s}_z \sin k_z - \hat{\sigma}_z B_3(2 - 2\cos k_z). \end{aligned} \quad (5)$$

In the rest of this study, we use the calligraphic font to describe the Hamiltonian for a fixed j. We performed numerical calculations using the Kwant code [38].

A superconducting system with vortex lines along the z direction can be considered a quasi-1D system, which belongs to class D of the Altland–Zirnbauer classification [39]. Notably, the particle-hole symmetry yields $\hat{P}\mathcal{H}^{(j)}\hat{P}^{-1} = -\mathcal{H}^{(-j)}$. Therefore, if the system is fully gapped, its topology is characterized by the $\mathbb{Z}_2$ topological invariant ν [1]:

$$\nu = \mathrm{sgn}\left\{\frac{\mathrm{Pf}[\mathcal{H}_{\mathrm{Mj}}^{(0)}(r_0, k_z = 0)]}{\mathrm{Pf}[\mathcal{H}_{\mathrm{Mj}}^{(0)}(r_0, k_z = \pi)]}\right\} \quad (6)$$

with $\mathcal{H}_{\mathrm{Mj}}^{(0)}$ the Hamiltonian $\mathcal{H}^{(j=0)}$ written in the Majorana basis. We plot the product of the topological invariant ν and the system gap amplitude E_{gap} as a function of r_0 and μ in Fig. 1(b), explicitly showing a TPT, characterized by the sign change of ν and gap closure. To further understand this TPT, at $\mu = 0$ with an open boundary condition along the z direction, we plot the energy spectrum [Fig. 1(c)] and lowest-energy wave function [Fig. 1(d)] with respect to the nanowire radius. The emergence of

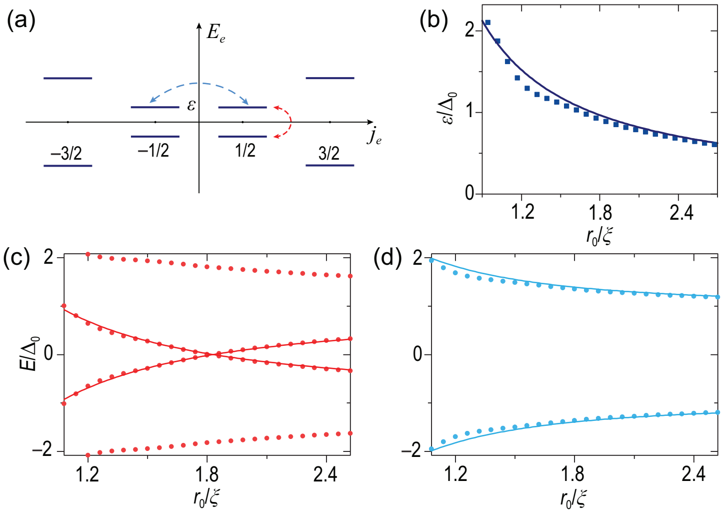

Figure 2. (a) The spectrum illustration of low-energy states of the electron Hamiltonian part $H_{\rm TI}$ from Equation (2) with $k_z=\pi$. (b) The lowest positive eigenenergy of the TI for $j_e=1/2$ and $k_z=\pi$. The curve is the approximate energy given by Equation (9). (c),(d) Low energies (dots) of the superconducting nanowire with $k_z=\pi$ in the presence or absence of a single vortex corresponding to the electron pair indicated by a red or cyan dashed line, respectively, in (a). The curves are approximate analytical energies given by Equations (8) and (10). The TI parameters are the same as those in Fig. 1.

the zero-energy mode above the critical radius $r_c\approx 1.8\xi\approx 10$ nm indicates a TPT and the MZM. As the radius decreases, the MZM wave function shifts toward the edge [also shown in Fig. 1(e)]. When the nanowire radius crosses the critical radius r_c, the MZMs on the upper and lower surfaces gradually couple through the lateral surface [Fig. 1(d)]. These suggest that the TPT is related to the surface states on the lateral boundary, which can be confirmed by studying the Hamiltonian of the system at the band inversion point $k_z=\pi$.

Notably, the corresponding electron Hamiltonian $H_{\rm TI}$ of Equation (2) always satisfies time-reversal symmetry; meanwhile, in Equation (1), only the superconducting gap function with one vortex $(n=1)$ breaks the time-reversal symmetry. Thus, the electronic spectrum [Fig. 2(a)] remains time-reversal invariant, say $E_{j_e}=E_{-j_e}$, with j_e the electronic angular momentum for $H_{\rm TI}$. For $n=1$, the time-reversal symmetry breaking is reflected in the fact that the Cooper pairs are formed by coupling two electrons with angular momentum $(j_e,-j_e+1)$ [indicated by the red dashed double arrows in Fig. 2(a)]. Considering $j_e=1/2$ as an example, the corresponding BdG Hamiltonian projected to $j_e=1/2$ sector states takes the form

$$H_{j_e=1/2}\approx\begin{pmatrix}\varepsilon(r_0)\hat{s}_z-\mu\hat{s}_0 & -i\hat{s}_y\Delta(r_0)\\ i\hat{s}_y\Delta(r_0) & -\varepsilon(r_0)\hat{s}_z+\mu\hat{s}_0\end{pmatrix},\tag{7}$$

which gives rise to the two lowest eigenenergies

$$E_\pm(r_0)=\pm[\varepsilon(r_0)-\sqrt{\Delta^2(r_0)+\mu^2}]\tag{8}$$

with

$$\varepsilon(r_0)=\frac{A}{2r_0}-\frac{B}{2r_0^2}\tag{9}$$

the eigenenergy in the electron spectrum [Fig. 2(b)] (see Sec. II within the online supplementary material for details). According to Equation (8), the BdG Hamiltonian of Equation (7) closes its gap at $\varepsilon(r_c)=\sqrt{\Delta^2(r_c)+\mu^2}$. In addition, the gap closing in other j_e sectors always occurs an even number of times because of the particle-hole symmetry. Therefore, the sector of $j_e=1/2$ determines the TPT. We numerically calculate and plot the four eigenenergies closest to zero as a function of r_0 with red dots when $\mu=0$ in Fig. 1(c), which agree with our analytical results (the red solid curves) obtained from Equation (8). In particular, ignoring the spatial variation of Δ, the critical point could be simplified as $r_c\approx A/(2\Delta_0)=\pi\xi/2$. As a comparison, for the superconducting nanowire without vortices $(n=0)$, the electron states will couple their time-reversal partner in SC [indicated by the blue double arrows in Fig. 2(a)], and the energies become

$$E_\pm(r_0)=\pm\sqrt{[\varepsilon(r_0)-\mu]^2+\Delta_0^2},\tag{10}$$

which is always fully opened by the superconducting gap [Fig. 2(d)], corresponding to no TPT and no topological region in the nanowire.

Notably, near the TPT, the lowest-energy wave functions always distribute at the nanowire boundary, which agrees with the small decay length of the lateral TI surface states of the electron Hamiltonian $l_e\approx 2$ (nm) $\ll r_c$. Therefore, the energy gap $\varepsilon(r_0)$ [Equation (9)] and TPT in the superconducting nanowire is not due to the overlap between the TI surface states. As the TPT occurs at the lateral surface, we find in Fig. 1(d) and (e) that, when r_0 is slightly greater than r_c, the MZMs can have a considerable weight on the edge. For example, in Fig. 1(e), when r_0 shrinks to the magnitude of 4ξ, the distribution of MZMs at the edges is larger than that at the center. This finite distribution of MZMs at edges will enable the coupling of two MZMs from parallel nanowires, which we discuss in the section after next.

LOCAL EFFECTIVE ZF AND EDGE MZMS

For thick iron-based superconducting nanowires or materials with short superconducting coherence length, the MZM wave function is mainly

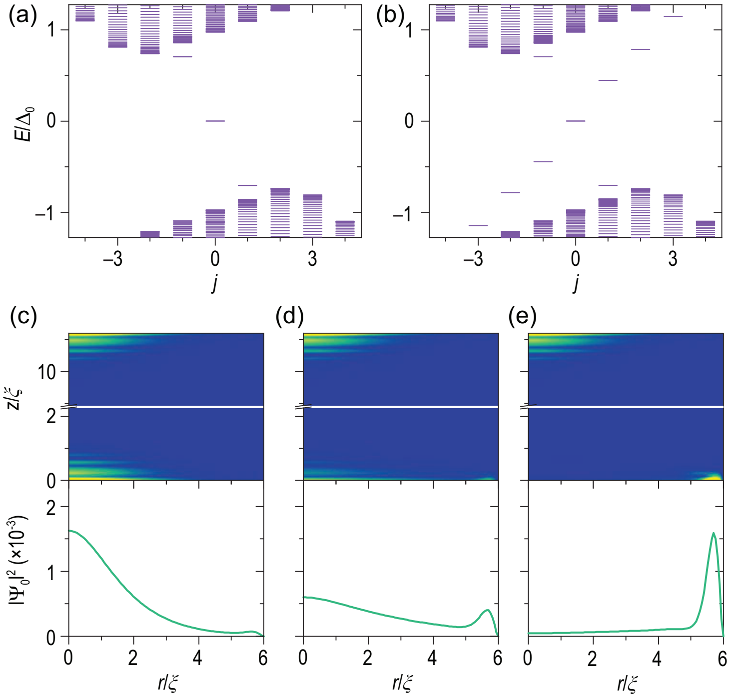

Figure 3. The spectra of the iron-based superconducting nanowire system in Equation (11) with the bottom layer effective ZF (a) $V_z = 0$ and (b) $V_z = 4\Delta_0$ at $\mu = 1.2\Delta_0$. (c)–(e) The MZM distribution $|\Psi_0|^2$ near the top and bottom surfaces corresponding to $V_z = 0, 2$ and $4\,(\Delta_0)$ in sequence. The lower panels show the probability density $|\Psi_0(r)|^2$ on the bottom surface. Other parameters are the same as those in Fig. 1.

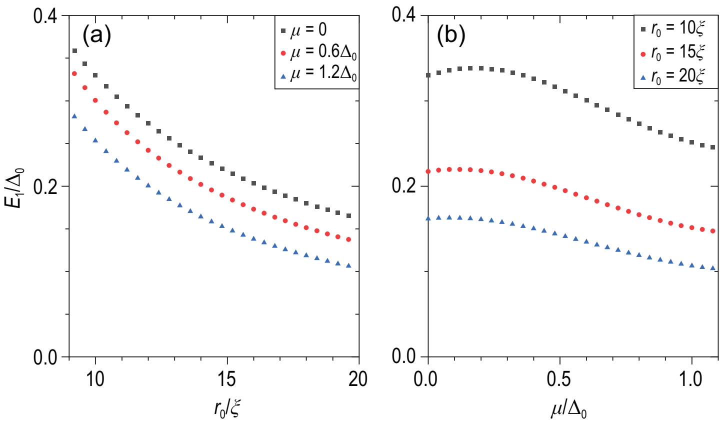

Figure 4. The scatter graphs of the first excited energy E_1 of the Hamiltonian in Equation (11) with respect to (a) the superconducting nanowire's radius r_0 for different chemical potentials and (b) the chemical potential μ for different radii of nanowires with $V_z = 4\Delta_0$. Other parameters are the same as those in Fig. 3.

concentrated in the vortex center, which is unfavorable for MZM manipulation. To improve MZM controllability, a local effective ZF is added at the bottom surface $\hat{V}_{\rm Z}(z) = -V_z\delta(z)\hat{\tau}_z\hat{s}_z$ to push the MZMs to the edge. We propose to use an intralayer ferromagnetic and interlayer antiferromagnetic substrate to generate the effective ZF through short-range exchange interactions without introducing the undesired magnetic field [40,41]. Then, the Hamiltonian of the iron-based superconducting nanowires becomes

$$\mathcal{H}^{(j)}(r,z) = \begin{pmatrix} \mathcal{H}_{\rm TI}^{(j)} + \hat{V}_{\rm Z} - \mu & -i\hat{s}_y\Delta_0\tanh(r/\xi) \\ i\hat{s}_y\Delta_0\tanh(r/\xi) & -\mathcal{H}_{\rm TI}^{(-j)^*} - \hat{V}_{\rm Z} + \mu \end{pmatrix}. \tag{11}$$

The local effective ZF changes the surface state energy gap from superconducting dominant to magnetic dominant at the bottom surface. In general, when $|V_z| > \sqrt{\Delta_0^2 + \mu^2}$, the superconductivity of this bottom surface will be completely suppressed. In this case, the MZM at the bottom surface will be distributed around the bottom edge, say the boundary between the insulating bottom surface and superconducting lateral surface. Therefore, the original vortex MZM becomes a chiral MZM [6,42,43]. This can be seen from the spectrum and MZM distribution of the nanowires in Fig. 3.

Without loss of generality, we consider a sufficiently long l_0 and $r_0 = 6\xi$ and $\mu = 1.2\Delta_0$. Obviously, with or without the effective ZF, the two MZMs were always degenerated at $j = 0$ and $E = 0$ [see Fig. 3(a) for $V_z = 0$ and Fig. 3(b) for $V_z = 4\Delta_0$]. Meanwhile, the bottom and top MZMs are well separated [Fig. 3(c)–(e)]. Tracing the wave function of MZMs with increasing V_z, the vortex MZM on the lower surface gradually becomes an edge mode [Fig. 3(c)–(e)]. Moreover, further comparing the energy spectrum with and without the effective ZF, we found that the ZF does yield extra in-gap states [Fig. 3(b)]. Notably, the energy difference between the MZMs and the first excited state gives the effective gap, which determines the upper limit of the ambient temperature and operating speed desired to manipulate the MZMs. Therefore, we plot the first excited state energy E_1, indicating the effective gap, versus the radius of the cylindrical model r_0 with a fixed wire length [Fig. 4(a)]. The excited energies become significantly quantized and E_1 grows close to half of Δ_0 as the radius r_0 shrinks to below 10ξ [44]. In addition, a lower chemical potential $|\mu|$ yields a larger energy gap. We also plot the energy gap versus μ for different cylindrical radii r_0 [Fig. 4(b)]. As $|\mu|$ moves farther away from the Dirac point of the topological surface states, the energy gap indeed reduces for any r_0 case. Notably, even if the radius changes to $r_0 = 20\xi \approx 100$ nm, the energy of the first excited state still has $0.1\Delta_0 \approx 0.18$ meV.

By neglecting the bulk states, we analytically calculated the approximate function of the excited energy (see Sec. III within the online supplementary

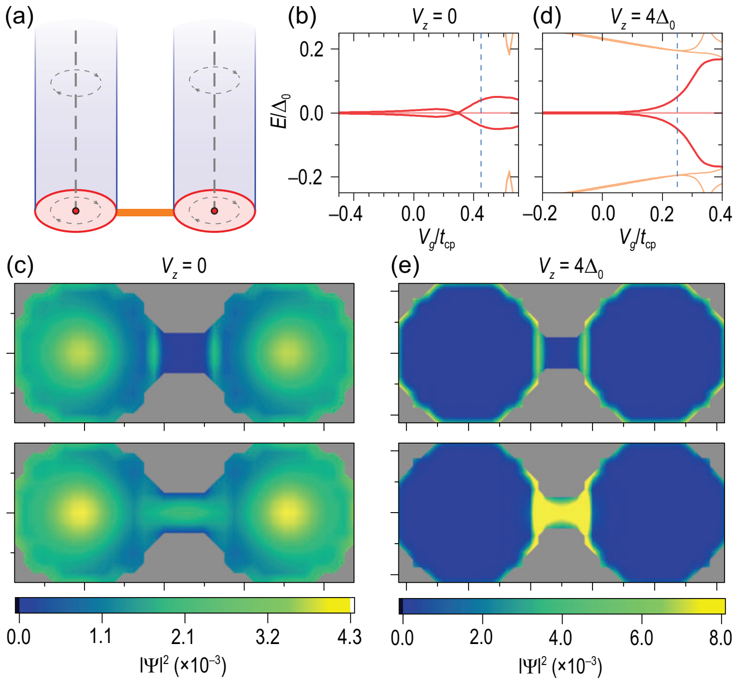

Figure 5. (a) Schematic of two coupled MZMs at the bottom of two parallel nanowires described by Equation (13). (b) Spectra of the two-nanowire system with radius $r_0 = 4\xi$ as a function of the potential on the connection V_g. (c) Probability density of two decoupled ($V_g = -0.5t_{\rm cp}$) and coupled ($V_g = 0.45t_{\rm cp}$, corresponding to the blue dashed line in the spectra) Majorana vortex states at the bottom layer. (d) Spectra of the two-nanowire system with effective local ZFs at the bottom surface. (e) Probability density of two decoupled ($V_g = -0.5t_{\rm cp}$) and coupled ($V_g = 0.25t_{\rm cp}$, the blue dashed line in the spectra) edge Majorana states induced by the effective local ZFs. The nanowire parameters are the same as those in Fig. 1, expect that $M = 4$ meV and lattice constants $\xi/2$ ($\xi/4$) perpendicular (parallel) to the z direction.

material for details)

$$\tilde{E}_1 \approx \frac{\pi}{\tilde{r}_0(1+\tilde{\mu}^2)} \quad (\tilde{r} \gg 1), \tag{12}$$

with the rescaled $\tilde{E}_1 = E_1/\Delta_0$, $\tilde{\mu} = \mu/\Delta_0$, $\tilde{r}_0 = r_0/\xi$. This approximate function confirms the changing trend of E_1, inversely proportional to r_0 and μ^2, in our iron-based superconducting nanowire system.

Notably, in the 2D vortex system, braiding MZMs can be achieved by tuning the coupling of the edge MZMs [31]. In that case, suppressing the coupling of edge chiral MZMs and vortex center MZMs requires increasing the distance between them, whereas ensuring a considerable energy gap between chiral MZMs and other edge states requires reducing the system size. In 2D topological SCs, these two contradictory conditions are difficult to reconcile because there is only one adjustable size parameter: the system radius. However, for iron-based superconducting nanowires, these two conditions correspond to two independently tunable parameters, nanowire length l_0 and radius r_0, respectively, and can thus be simultaneously satisfied. These reflect the unique advantages of the iron-based superconducting nanowire system.

COUPLED TWO-EDGE MZMS

The core for braiding edge MZMs is to control the coupling between different MZMs [31]. To verify the feasibility of such a scheme in the iron-based superconducting nanowires, we explore the coupling of two MZMs at the end of two wires [Fig. 5(a)], whose Hamiltonian takes the form

$$H_{\rm tot} = H_{\rm S} + H_{\rm N} + H_{\rm NS}, \tag{13}$$

where $H_{\rm S}$ denotes the iron-based SC system given in Equation (1). Because of the lack of rotational symmetry, we now use a 3D tight-binding model with a cubic lattice. In $H_{\rm S}$, we adjust some parameters to facilitate the calculation, without changing the topological property. The two-vortex superconducting order parameter is set as

$$\Delta(\boldsymbol{r}) = \Delta_0 \tanh\frac{r_1}{\xi}e^{i\varphi_1}\tanh\frac{r_2}{\xi}e^{i\varphi_2}, \tag{14}$$

where r_i and $\varphi_i (i \in \{1,2\})$ denote the horizontal distances and azimuth angles measured from the vortex lines in the two nanowires, respectively. Any closed loop containing n vortex lines changes the phase of $\Delta(\boldsymbol{r})$ by $2n\pi$. A gate-tunable Sm lead connects the two nanowires from the bottom edge. We simulate the lead as a square lattice

$$H_{\rm N} = t_{\rm cp}\hat{\tau}_z(4 - 2\cos k_x - 2\cos k_y) - V_g, \tag{15}$$

and attach it to the superconducting nanowires with

$$H_{\rm NS} = -t_{\rm cp}\sum_{\alpha}(c^{\dagger}_{{\rm N}\alpha}\hat{\tau}_z c_{{\rm S}\bar{\alpha}} + {\rm H.c.}), \tag{16}$$

where $\bar{\alpha}$ denotes the sites at the nanowire edge attaching the ends α of the lead. The hopping strength is set as $t_{\rm cp} = 15$ meV. In addition, V_g denotes an adjustable on-site potential controlled by the gate voltage.

For the thin superconducting nanowires with diameters $d_0 = 8\xi \approx 42$ nm, the MZMs have finite distributions at the edges, as we mentioned in the section before last. Varying the potential V_g, we plot the low-energy spectrum of the system [Fig. 5(b)]. For $V_g \ll 0$, where the Fermi level is far away from the energy band bottom in the connecting lead, the wave functions of two bottom MZMs are disconnected, as shown in the upper panel of Fig. 5(c). In addition, their energies keep zeros, degenerating with the two vortex center MZMs on the top surfaces. Adjusting the potential to $V_g = 0.45t_{\mathrm{cp}}$, the two MZMs open a clear energy gap of about $0.04\Delta_0 \approx 0.07$ meV but still away from the excited states to avoid information leakage [Fig. 5(b)]. Meanwhile, parts of the two bottom MZMs penetrate the connecting lead and couple, as shown in the lower panel of Fig. 5(c). Moreover, the MZMs on the top are unaffected.

For the thicker superconducting nanowires, the weight of MZMs at the edges and the coupling by the connecting lead will be lower. However, we could enhance the coupling by adding an effective ZF $V_z = 4\Delta_0$ at the bottom surface, as we discussed in the previous section. We now consider nanowires of diameters $d_0 = 10\xi$ with local effective ZFs as an example. The variations in the spectrum and MZM wave functions are shown in Fig. 5(d)–(e). Similarly, the two-edge MZMs can be isolated or connected under the gate V_g adjustment. Although some in-gap interferential edge states are induced by the effective ZF, the energies of the coupled edge MZMs grow exponentially away from the degenerated zero-energy space as V_g increases under the excited states.

RESTRICTIONS ON THE NUMBER OF VORTICES

So far, we have assumed that each superconducting nanowire contains only one vortex. If there are two vortices with the same chirality in the nanowire, the nanowire diameter will limit the distance separating them, which will cause a finite repulsive potential and increase the system's free energy. Therefore, it is not surprising that repulsive interactions limit the number of vortices that penetrate the nanowire. The contribution of the vortices to the free energy, through their induced magnetic fields $\boldsymbol{h}(\boldsymbol{r})$, can be expressed as [45]

$$\Delta F = \frac{1}{8\pi}\int [|\boldsymbol{h}(\boldsymbol{r})|^2 + |\nabla \times \boldsymbol{h}(\boldsymbol{r})|^2] d^3\boldsymbol{r}. \tag{17}$$

When there is one vortex in the system with rotational symmetry along the z direction, the increased free energy is

$$\Delta F_1 = \frac{\Phi_0 L}{8\pi} h_1(\xi), \tag{18}$$

where, in the range $r \in (\xi, \lambda)$, the induced magnetic field takes the form

$$h_1(r) \approx \frac{\Phi_0}{2\pi\lambda^2}\left(\ln\frac{\lambda}{r} + 0.12\right) \tag{19}$$

with λ the penetration depth of the magnetic field. When there are two vortices in the system, the induced magnetic field can be considered as the superposition of the magnetic field induced by each vortex [45]. Therefore, the increased free energy of the two vortices can be estimated as

$$\Delta F_2 = 2\Delta F_1 + \frac{\Phi_0 L}{4\pi} h_1(2r_0), \tag{20}$$

where the second term on the right-hand side is from the interaction of the two vortices separated by the maximum distance $2r_0$ inside the nanowire cross section.

Moreover, when the second vortex starts to appear in the system, the lower critical fields $H_{\mathrm{c1}}^{(n=1,\,2)}$ satisfy the conditions [45] (see Sec. IV within the online supplementary material for details)

$$\Delta F_1 = \frac{\int \boldsymbol{H}_{\mathrm{c1}}^{(n=1)} \cdot \boldsymbol{h}\, d^3\boldsymbol{r}}{4\pi} = H_{\mathrm{c1}}^{(n=1)}\frac{\Phi_0 L}{4\pi}, \tag{21}$$

$$\Delta F_2 - \Delta F_1 = H_{\mathrm{c1}}^{(n=2)}\frac{\Phi_0 L}{4\pi}. \tag{22}$$

Substituting Equations (18) and (20) into Equations (21) and (22), we have

$$\delta H = H_{\mathrm{c1}}^{(n=2)} - H_{\mathrm{c1}}^{(n=1)} = H_{\mathrm{c1}}^{(n=1)}\frac{2h_1(2r_0)}{h_1(\xi)}. \tag{23}$$

Clearly, the δH is not negligible for small size, and it becomes larger as the distance between vortices becomes more restricted. For nanowires with $2r_0 \in (\xi, \lambda)$, according to Equation (19), δH can be estimated as

$$\frac{\delta H}{H_{\mathrm{c1}}^{(n=1)}} \approx 2\left[1 - \frac{\ln 2\tilde{r}_0}{\ln\kappa}\right] \tag{24}$$

with $\tilde{r}_0 = r_0/\xi$ and $\kappa = \lambda/\xi$ as the dimensionless Ginzburg–Landau parameter. As shown in Fig. 6, materials with larger κ and made into thinner nanowires have larger δH. Particularly for Fe(Se,Te), which satisfies $\kappa \approx 10^2$ [46] with r_0 about dozens of ξ, δH is of a similar magnitude as H_{c1}. Thus, we can control the external magnetic field

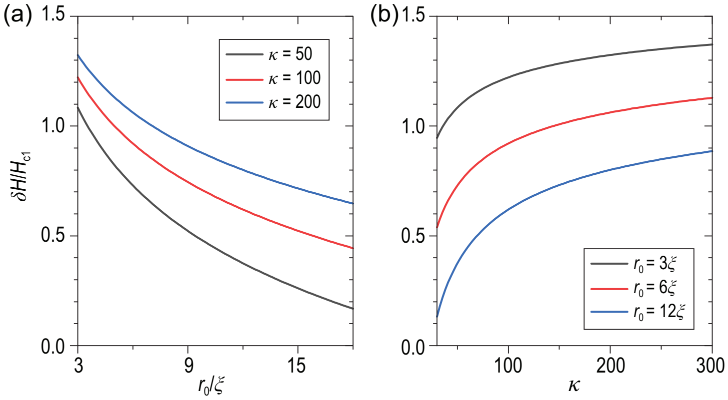

Figure 6. The estimated range of magnetic fields δH when only a single vortex penetrates the system as a function of (a) the nanowire radius r_0 and (b) the dimensionless Ginzburg–Landau parameter κ.

in the range $(H_{c1}, H_{c1} + \delta H)$ to manufacture single vortex nanowires and prepare stable edge MZMs.

CONCLUSION AND DISCUSSION

In this study, we propose an iron-based superconducting nanowire system to achieve controlled MZM. The finite radius of the nanowires limits the number of vortices penetrating them and stabilizes the ground-state degeneracy of the Majorana platform within a certain range of external magnetic fields. We found a size effect-induced TPT when the diameter of the iron-based superconducting nanowires is reduced to about $\pi\xi$, approximately 20 nm for the Fe(Se,Te) nanowire, which yields a lower bound for the nanowire diameter. When the diameter is about $(\pi\xi, 4\pi\xi)$, the MZMs have a limited distribution not only in the vortex center but also at the edges. For thick nanowires, edge MZMs can be obtained by inducing local effective ZFs, whereas the excitation energy of the disturbed edge states can be quantified by reducing the radius or decreasing the chemical potential. The edge MZMs in the nanowires can be connected in parallel by tunable Sm wires as a key step to achieving MZM manipulation.

As of now, the superconducting nanowires in the (100) direction have been fabricated [47–49]. The iron-based SCs have a strong TI band structure. Therefore, our theory is qualitatively applied to the (100)-direction nanowires; the details will be provided in future work. In most experimental studies, the fabrication control of impurities is necessary to tune the chemical potential but may lower the wire quality. A recent experimental study showed that applying strains in a suitable direction can tune the chemical potential in LiFeAs [50], which suggests a new technique of chemical potential control other than impurity doping. Thus, iron-based superconducting nanowires provide a promising platform for achieving controllable MZMs and studying MZM's non-Abelian properties.

SUPPLEMENTARY DATA

Supplementary data are available at *NSR* online.

ACKNOWLEDGEMENTS

We would like to thank Ching-Kai Chiu, Gang Xu, Yi Zhou, Xiao Hu, Ling-Yuan Kong and Hong Ding for fruitful discussions.

FUNDING

X.L. acknowledges support from the National Natural Science Foundation of China (NSFC) (12074133), the NSFC (11674114), and the National Key R&D Program of China (2016YFA0401003). F.-C.Z. is partially supported by the NSFC (11674278), the Priority Program of Chinese Academy of Sciences (XDB28000000), and the Innovation Program for Quantum Science and Technology of Ministry of Science and Technology of China (2021ZD0302500). D.E.L. is supported by the NSFC (11974198).

AUTHOR CONTRIBUTIONS

X.L., F.-C.Z. and D.E.L. initialized the idea and started this research. C.L. carried out the calculations under X.L.'s supervision. X.-J.L. and L.C. provided calculation assistance. All authors contributed to writing the manuscript.

Conflict of interest statement. None declared.

REFERENCES

1. Kitaev AY. Unpaired Majorana fermions in quantum wires. *Phys-Usp* 2001; **44**: 131–6.
2. Sato M, Takahashi Y and Fujimoto S. Non-Abelian topological order in s-wave superfluids of ultracold fermionic atoms. *Phys Rev Lett* 2009; **103**: 020401.
3. Lutchyn RM, Sau JD and Das Sarma S. Majorana fermions and a topological phase transition in semiconductor-superconductor heterostructures. *Phys Rev Lett* 2010; **105**: 077001.
4. Oreg Y, Refael G and von Oppen F. Helical liquids and Majorana bound states in quantum wires. *Phys Rev Lett* 2010; **105**: 177002.
5. Read N and Green D. Paired states of fermions in two dimensions with breaking of parity and time-reversal symmetries and the fractional quantum Hall effect. *Phys Rev B* 2000; **61**: 10267–97.
6. Fu L and Kane CL. Superconducting proximity effect and Majorana fermions at the surface of a topological insulator. *Phys Rev Lett* 2008; **100**: 096407.
7. Sau JD, Lutchyn RM and Tewari S *et al.* Generic new platform for topological quantum computation using semiconductor heterostructures. *Phys Rev Lett* 2010; **104**: 040502.

8. Mourik V, Zuo K and Frolov SM *et al.* Signatures of Majorana fermions in hybrid superconductor-semiconductor nanowire devices. *Science* 2012; **336**: 1003–7.
9. Deng MT, Yu CL and Huang GY *et al.* Anomalous zero-bias conductance peak in a Nb–InSb nanowire–Nb hybrid device. *Nano Lett* 2012; **12**: 6414–9.
10. Das A, Ronen Y and Most Y *et al.* Zero-bias peaks and splitting in an Al–InAs nanowire topological superconductor as a signature of Majorana fermions. *Nat Phys* 2012; **8**: 887–95.
11. Nichele F, Drachmann ACC and Whiticar AM *et al.* Scaling of Majorana zero-bias conductance peaks. *Phys Rev Lett* 2017; **119**: 136803.
12. Choy TP, Edge JM and Akhmerov AR *et al.* Majorana fermions emerging from magnetic nanoparticles on a superconductor without spin-orbit coupling. *Phys Rev B* 2011; **84**: 195442.
13. Nadj-Perge S, Drozdov IK and Li J *et al.* Observation of Majorana fermions in ferromagnetic atomic chains on a superconductor. *Science* 2014; **346**: 602–7.
14. Wang MX, Liu C and Xu JP *et al.* The coexistence of superconductivity and topological order in the Bi_2Se_3 thin films. *Science* 2012; **336**: 52–5.
15. Sun HH, Zhang KW and Hu LH *et al.* Majorana zero mode detected with spin selective Andreev reflection in the vortex of a topological superconductor. *Phys Rev Lett* 2016; **116**: 257003.
16. Hu LH, Li C and Xu DH *et al.* Theory of spin-selective Andreev reflection in the vortex core of a topological superconductor. *Phys Rev B* 2016; **94**: 224501.
17. Krogstrup P, Ziino NLB and Chang W *et al.* Epitaxy of semiconductor–superconductor nanowires. *Nat Mater* 2015; **14**: 400–6.
18. Frolov SM, Manfra MJ and Sau JD. Topological superconductivity in hybrid devices. *Nat Phys* 2020; **16**: 718–24.
19. Machida T, Sun Y and Pyon S *et al.* Zero-energy vortex bound state in the superconducting topological surface state of Fe(Se,Te). *Nat Mater* 2019; **18**: 811–5.
20. Wang D, Kong L and Fan P *et al.* Evidence for Majorana bound states in an iron-based superconductor. *Science* 2018; **362**: 333–5.
21. Chen M, Chen X and Yang H *et al.* Discrete energy levels of Caroli-de Gennes-Matricon states in quantum limit in $Fe(Te_{0.55}Se_{0.45})$. *Nat Commun* 2018; **9**: 970.
22. Liu Q, Chen C and Zhang T *et al.* Robust and clean Majorana zero mode in the vortex core of high-temperature superconductor $(Li_{0.84}Fe_{0.16})OHFeSe$. *Phys Rev X* 2018; **8**: 041056.
23. Kong L, Zhu S and Papaj M *et al.* Half-integer level shift of vortex bound states in an iron-based superconductor. *Nat Phys* 2019; **15**: 1181–7.
24. Zhang P, Wang Z and Wu X *et al.* Multiple topological states in iron-based superconductors. *Nat Phys* 2019; **15**: 41–7.
25. Chen C, Liu Q and Zhang TZ *et al.* Quantized conductance of Majorana zero mode in the vortex of the topological superconductor $(Li_{0.84}Fe_{0.16})OHFeSe$. *Chin Phys Lett* 2019; **36**: 057403.
26. Liu W, Cao L and Zhu S *et al.* A new Majorana platform in an Fe-As bilayer superconductor. *Nat Commun* 2020; **11**: 5688.
27. Zhang T, Bao W and Chen C *et al.* Observation of distinct spatial distributions of the zero and nonzero energy vortex modes in $(Li_{0.84}Fe_{0.16})OHFeSe$. *Phys Rev Lett* 2021; **126**: 127001.
28. Ivanov DA. Non-Abelian statistics of half-quantum vortices in p-wave superconductors. *Phys Rev Lett* 2001; **86**: 268–71.
29. Alicea J, Oreg Y and Refael G *et al.* Non-Abelian statistics and topological quantum information processing in 1D wire networks. *Nat Phys* 2011; **7**: 412–7.
30. Sau JD, Clarke DJ and Tewari S. Controlling non-Abelian statistics of Majorana fermions in semiconductor nanowires. *Phys Rev B* 2011; **84**: 094505.
31. Liang QF, Wang Z and Hu X. Manipulation of Majorana fermions by point-like gate voltage in the vortex state of a topological superconductor. *Europhys Lett* 2012; **99**: 50004.
32. Liu X, Li X and Deng DL *et al.* Majorana spintronics. *Phys Rev B* 2016; **94**: 014511.
33. Karzig T, Knapp C and Lutchyn RM *et al.* Scalable designs for quasiparticle-poisoning-protected topological quantum computation with Majorana zero modes. *Phys Rev B* 2017; **95**: 235305.
34. Hosur P, Ghaemi P and Mong RSK *et al.* Majorana modes at the ends of superconductor vortices in doped topological insulators. *Phys Rev Lett* 2011; **107**: 097001.
35. Xu G, Lian B and Tang P *et al.* Topological superconductivity on the surface of Fe-based superconductors. *Phys Rev Lett* 2016; **117**: 047001.
36. Qin S, Hu L and Wu X *et al.* Topological vortex phase transitions in iron-based superconductors. *Sci Bull* 2019; **64**: 1207–14.
37. Li C, Hu LH and Zhang FC. Hexagonal warping effect on Majorana zero modes at the ends of superconducting vortex lines in doped strong 3D topological insulators. *Sci China Phys Mech Astron* 2019; **62**: 117411.
38. Groth CW, Wimmer M and Akhmerov AR *et al.* Kwant: a software package for quantum transport. *New J Phys* 2014; **16**: 063065.
39. Chiu CK, Teo JCY and Schnyder AP *et al.* Classification of topological quantum matter with symmetries. *Rev Mod Phys* 2016; **88**: 035005.
40. Wu Y, Yin G and Pan L *et al.* Large exchange splitting in monolayer graphene magnetized by an antiferromagnet. *Nat Electron* 2020; **3**: 604–11.
41. Li N, Zhang J and Xue Y *et al.* Large valley polarization in monolayer $MoTe_2$ on a magnetic substrate. *Phys Chem Chem Phys* 2018; **20**: 3805–12.
42. Pan XH, Yang KJ and Chen L *et al.* Lattice-symmetry-assisted second-order topological superconductors and Majorana patterns. *Phys Rev Lett* 2019; **123**: 156801.
43. Wu X, Chung SB and Liu C *et al.* Topological orders competing for the Dirac surface state in FeSeTe surfaces. *Phys Rev Res* 2021; **3**: 013066.
44. Akzyanov RS, Rakhmanov AL and Rozhkov AV *et al.* Majorana fermions at the edge of superconducting islands. *Phys Rev B* 2015; **92**: 075432.
45. Tinkham M. *Introduction to Superconductivity*. New York: McGraw-Hill, 1996.
46. Kim H, Martin C and Gordon RT *et al.* London penetration depth and superfluid density of single-crystalline $Fe_{1+y}(Te_{1-x}Se_x)$ and $Fe_{1+y}(Te_{1-x}S_x)$. *Phys Rev B* 2010; **81**: 180503.
47. Mishra S, Song K and Koza JA *et al.* Synthesis of superconducting nanocables of FeSe encapsulated in carbonaceous shell. *ACS Nano* 2013; **7**: 1145–54.
48. Chen TK, Chang CC and Tang HY *et al.* Structural characteristics and phase separation of superconducting $Fe_{1+y}Se_{1-x}Te_x$ nanowires. *Mater Res Express* 2014; **1**: 015026.
49. Tao YR, Fan L and Wu ZY *et al.* Synthesis and characterization of superconducting FeSe nanowires. *J Alloy Compd* 2018; **751**: 20–7.
50. Liu W, Hu Q and Wang X *et al.* Tunable vortex Majorana modes controlled by strain in homogeneous LiFeAs. arXiv: 2111.03786.